Earth System
Dynamics

MIROC6 Large Ensemble (MIROC6-LE): experimental design and initial analyses

Hideo Shiogama[1], Hiroaki Tatebe[2], Michiya Hayashi[1], Manabu Abe[2], Miki Arai[3], Hiroshi Koyama[2], Yukiko Imada[3], Yu Kosaka[4], Tomoo Ogura[1], and Masahiro Watanabe[3]

[1]Earth System Division, National Institute for Environmental Studies, Tsukuba, 305-8506, Japan
[2]Japan Agency for Marine-Earth Science and Technology, Yokohama, 236-0001, Japan
[3]Atmosphere and Ocean Research Institute, University of Tokyo, Kashiwa, 277-8564, Japan
[4]Research Center for Advanced Science and Technology, University of Tokyo, Tokyo, 153-8904, Japan

Correspondence: Hideo Shiogama (shiogama.hideo@nies.go.jp)

Abstract. Single model initial-condition large ensembles (LEs) are a useful approach to understand the roles of forced responses and internal variability in historical and future climate change. Here, we produce one of the largest ensembles thus far using the MIROC6 coupled atmosphere–ocean global climate model (MIROC6-LE). The total experimental period of MIROC6-LE is longer than 76 000 years. MIROC6-LE consists of a long preindustrial control run, 50-member historical simulations, 8 single forcing historical experiments with 10 or 50 members, 5 future scenario experiments with 50 members and 3 single forcing future experiments with 50 members. Here, we describe the experimental design. The output data of most of the experiments are freely available to the public. This dataset would be useful to a wide range of research communities.

We also demonstrate some examples of initial analyses. Specifically, we confirm that the linear additivity of the forcing-response relationship holds for the 1850–2020 trends of the annual mean values and extreme indices of surface air temperature and precipitation by analyzing historical fully forced runs and the sum of single forced historical runs. To isolate historical anthropogenic signals of annual mean and extreme temperature for 2000–2020 relative to 1850–1900, ensemble sizes of 4 and 15, respectively, are sufficient in most of the world. Historical anthropogenic signals of annual mean and extreme precipitation are significant with the 50-member ensembles in 76 % and 69 % of the world, respectively. Fourteen members are sufficient to examine differences in changes in annual mean values and extreme indices of temperature and precipitation between the shared socioeconomic pathways (ssp), ssp585 and ssp126, in most of the world. Ensembles larger than 50 members are desirable for investigations of differences in annual mean and extreme precipitation changes between ssp126 and ssp119.

Historical and future changes in internal variability, represented by departures from the ensemble mean, are analyzed with a focus on the El Niño/Southern Oscillation (ENSO) and global annual mean temperature and precipitation. An ensemble size of 31 is large enough to detect ENSO intensification from preindustrial conditions to 1951–2000, from 1951–2000 to 2051–2100 in all future experiments, and from low- to high-emission future scenario experiments. The single forcing historical experiments with 27 members can isolate ENSO intensification due to anthropogenic greenhouse gas and aerosol forcings. Future changes in the global mean temperature variability are discernible with 23 members under all future experiments, while 50 members are not sufficient for detecting changes in the global mean precipitation variability in ssp119 and ssp126. We also confirm that these temperature and precipitation variabilities are not precisely analyzed when detrended anomalies from the long-term averages are used due to interannual climate responses to the historical natural forcing, which highlights the importance of large ensembles for assessing internal variability.

1 Introduction

Internal variability in the climate system is one of the major sources of uncertainty in future climate change projections, especially at the near-term and regional scales (Hawkins and Sutton, 2011; Lehner et al., 2020). Because single model initial-condition large ensembles (LEs) can provide climate scientists with useful tools for quantifying and separating the internal variability of the climate system from the responses to external forcing, some modeling centers around the world have recently produced LEs using coupled atmosphere–ocean global climate models (CGCMs). For example, the Community Earth System Model Large Ensemble Project generated a 40-member ensemble simulation of the historical period (1920–2005) and a representative concentration pathway (RCP) 8.5 scenario (2006–2100) using the CESM1 model (CESM1-LE; Kay et al., 2015). By using CESM2, Rodgers et al. (2021) ran a 100-member ensemble for the 1850–2100 period with historical (1850–2014) and SSP3-7.0 (2015–2100) forcings (CESM2-LE). The Max Planck Institute Grand Ensemble (MPI-GE) consists of an 800-year preindustrial condition run, 100-member ensembles over the historical period (1850–2005), 3 RCPs (RCP2.6, 4.5, and 8.5 for 2006–2099) and simulations with a 1 % yr^{-1} CO$_2$ increase (150 years) using the MPI-ESM1.1 model (Maher et al., 2019). The Swedish Meteorological and Hydrological Institute used the EC-Earth3 model to generate 50-member ensembles over the historical interval (1970–2014) and four shared socioeconomic pathway simulations (2015–2100; SSP1-1.9, SSP3-3.4, SSP5-3.4-OS, and SSP5-8.5) (SMHI-LENS; Wyser et al., 2021). Lin et al. (2022) computed 110-member ensemble simulations for the historical period and SSP5-8.5 scenario using the FGOALS-g3 CGCM.

In addition to historical all forcing runs, single forcing historical experiments are important for detection and attribution studies of historical climate changes and for understanding the role of internal variability in observed historical climate changes (Gillett et al., 2021; Watanabe et al., 2014, 2021; Shiogama et al., 2016). The CESM1 Single Forcing Large Ensemble Project produced three "all but one" type ensembles, which kept anthropogenic aerosols (20 members), biomass burning aerosols (15), or greenhouse gases (20) fixed at the 1920 condition while all other external anthropogenic and natural forcing factors evolved following historical and RCP8.5 scenarios (Deser et al., 2020). To contribute to the Detection and Attribution Model Intercomparison Project (DAMIP; Gillett et al., 2016; 2021), which is one of the endorsed model intercomparison projects (MIPs) of Coupled Model Intercomparison Project Phase 6 (CMIP6; Eyring et al., 2016), the CNRM-CM6-1, CanESM5, GISS-E2-1-G, IPSL-CM6A-LR, and MIROC6 models have generated ensembles of single forcing historical experiments con-

sidering changes in the well-mixed greenhouse gas only, the anthropogenic aerosol emissions only, and the natural forcing (solar and volcanic activities) only (these are Tier 1 experiments from DAMIP) with ensemble sizes ≥ 10. The other models provided the outputs of smaller ensembles. (Note that the minimum ensemble size required by DAMIP is 3.) Under the auspices of the Lighthouse Activity on Explaining and Predicting Earth System Change (LHA-EPESC) initiative from the World Climate Research Programme, Smith et al. (2022) recently proposed the Large Ensemble Single Forcing Model Intercomparison Project (LESFMIP). LESFMIP calls on modeling centers around the world to enlarge the ensemble sizes of historical single forcing experiments from DAMIP and to perform several "all but one" type experiments to improve the understanding of the causes of past climate changes on multiannual to decadal time scales.

By using the MIROC6 CGCM (Tatebe et al., 2019), we produced a large ensemble named MIROC6-LE. MIROC6-LE consists of an 800-year preindustrial condition run, 50-member historical simulations, 8 single forcing historical simulations with 10 or 50 members, 5 SSP simulations with 50 members and 3 single forcing ssp245 simulations with 50 members. This is one of the largest LEs currently available. The aim of this paper is to describe the design of MIROC6-LE and to show some examples of analyses.

2 Experimental designs

We used the MIROC6 CGCM (Tatebe et al., 2019), which contributed to CMIP6. The atmospheric component has an approximate horizontal resolution of 1.4° and consists of 81 vertical levels. The ocean component has an approximate horizontal resolution of 1° and 63 vertical levels. We increased the ensemble sizes of the CMIP6 simulations and performed an experiment recently proposed by Smith et al. (2022).

We computed 50-member historical simulations (1850–2014) using the CMIP6 forcing dataset (Table 1). The initial conditions for the atmosphere, land, and ocean are taken from the different years (Table 2) of the 800-year stable preindustrial control run, which was run under the 1850 external forcing conditions (piControl) (Fig. 3 of Tatebe et al., 2019). To understand historical climate change, we performed large ensemble simulations of the DAMIP single forcing historical experiments (1850–2020; Gillett et al., 2016). These consist of the 50-member historical simulation experiments that used well-mixed greenhouse gases only (hist-GHG), natural forcing (solar and volcanic) only (hist-nat), and anthropogenic aerosol only (hist-aer), which are Tier 1 in DAMIP; and the 10-member ensembles of volcanic only (hist-volc), solar only (hist-sol), stratospheric ozone only (hist-stratO3), and stratospheric and tropospheric ozone only (hist-totalO3) experiments, which are Tiers 2 or 3 in

Table 1. List of historical experiments. Note that an 800-year preindustrial control run under the 1850 forcing condition is also included in MIROC6-LE.

Exp name	Forcing	Ens. size	Start year	End year	MIP (Tier)
historical	Anthropogenic and natural external forcing	50	1850	2014	CMIP6 DECK (1) LESFMIP (3)
hist-nat	Natural external forcing only	50	1850	2020	DAMIP (1) LESFMIP (3)
hist-GHG	Well-mixed GHG only	50	1850	2020	DAMIP (1) LESFMIP (1)
hist-aer	Anthropogenic aerosols only	50	1850	2020	DAMIP (1) LESFMIP (1)
hist-volc	Volcanic only	10	1850	2020	DAMIP (3) LESFMIP (1)
hist-sol	Solar only	10	1850	2020	DAMIP (3) LESFMIP (1)
hist-stratO3	Stratospheric ozone only	10	1850	2020	DAMIP (2)
hist-totalO3	Stratospheric and tropospheric ozone only	10	1850	2020	DAMIP (3) LESFMIP (1)
hist-lu	Land-use and land-cover change only	10	1850	2020	LESFMIP (1)

DAMIP. Although biomass burning aerosol emissions include both anthropogenic and natural components, anomalies from piControl (involving the 1850 emission of biomass burning aerosols) can be used to estimate the anthropogenic component. We computed historical simulations of land-use and land-cover change only (hist-lu, 10 members) proposed by LESFMIP.

We performed future projections (2015–2100) with 50 ensemble members under each of the five SSPs (Table 3): ssp585, ssp370, ssp245, and ssp126 are the Tier 1 experiments of the Scenario Model Intercomparison Project (ScenarioMIP; O'Neill et al., 2016), while ssp119 is Tier 2. Well-mixed greenhouse gases only (ssp245-GHG), aerosol only (ssp245-aer), and natural only (ssp245-nat) runs under the SSP2-4.5 scenario (proposed by DAMIP) and have been expanded to 50 members.

Here, we analyze the annual mean surface air temperature (T), annual mean precipitation (P), annual maximum daily maximum surface air temperature, (T_x) and annual maximum daily precipitation (P_x). The monthly mean sea surface temperature (SST) is also analyzed in Sect. 3.3.

3 Results

3.1 Historical experiments

Figure 1 shows the global mean changes in T and T_x for the historical simulations. Increases in greenhouse gas concentrations (hist-GHG) lead to larger degrees of warming than from the historical runs. Cooling due to anthropogenic aerosol emissions (hist-aer: sulfate, black carbon, and organic carbon aerosols are considered) partly compensates for GHG-induced warming. Although large volcanic activities can cause significant cooling within a few years, natural forcing does not induce long-term trends (hist-nat, hist-sol, and hist-volc). Changes in stratospheric and tropospheric ozone (hist-stratO3 and hist-totalO3) and land use and land cover (hist-lu) have small effects on the global mean T and T_x: changes in stratospheric ozone and land use and land cover

have small cooling effects in the second half of the 20th century and changes in total ozone have small warming effects.

Figure 2 presents the global mean changes in P and P_x for the historical simulations. Because P is sensitive to aerosols (Shiogama et al., 2010a, b), decreases in P due to aerosols (hist-aer in Fig. 2a) mostly compensate for the GHG-induced increases in P (hist-GHG) (Wu et al., 2013; Shiogama et al., 2022). Therefore, the P of the historical runs only has a small trend. In contrast, the magnitude of the decrease in P_x due to anthropogenic aerosols (hist-aer in Fig. 2d) is less than the increases in P_x due to greenhouse gases (hist-GHG), which results in a positive trend of P_x in the historical runs. Large volcanic eruptions cause significant decreases in P and P_x within a few years (Iles and Hegerl, 2014), but volcanic and solar forcing do not cause long-term trends (hist-nat, hist-sol, and hist-volc). Changes in P and P_x due to stratospheric and tropospheric ozone are small (hist-stratO3 and hist-totalO3). It is interesting that changes in land use and land cover cause slightly negative trends of P (hist-lu). Global mean annual mean precipitation must be equal to global mean annual mean evaporation at the surface. Deforestation reduces evaporation and thereby precipitation (Devaraju et al., 2015). Changes in extreme precipitation are not necessarily controlled by such a balance between precipitation and evaporation (Sugiyama et al., 2010).

Detection and attribution studies have explicitly or implicitly assumed that individual climate responses to individual forcing agents can be linearly added to obtain the total climate response to the combined forcing agents (Shiogama et al., 2013). We test this assumption of the linear additivity of the forcing-response relationship (Fig. 3). We examine the 1850–2020 trends (2015–2020 are under SSP2-4.5) of T, P, T_x, and P_x averaged over the world and the 26 land regions defined by the IPCC (2012). Orange boxes indicate the min–max ranges of 1000 ensemble average values for randomly sampled 50-member historical runs with replacement. We randomly select M ensemble members from each of the hist-GHG, hist-aer, hist-totalO3, hist-lu, hist-sol, and hist-volc experiments 1000 times with replacement (M is the ensemble size for each

Table 2. List of initial conditions for each ensemble member of historical and DAMIP experiments. We took initial conditions at 1 January of the branch years of the piControl run.

| #	1	2	3	4	5	6	7	8	9	10
Branch year	0	30	60	90	120	150	180	210	240	270
#	11	12	13	14	15	16	17	18	19	20
Branch year	300	330	360	390	420	450	480	510	540	570
#	21	22	23	24	25	26	27	28	29	30
Branch year	600	620	640	660	680	700	720	740	760	780
#	31	32	33	34	35	36	37	38	39	40
Branch year	10	20	40	50	70	80	100	110	130	140
#	41	42	43	44	45	46	47	48	49	50
Branch year	610	630	650	670	690	710	730	750	770	790
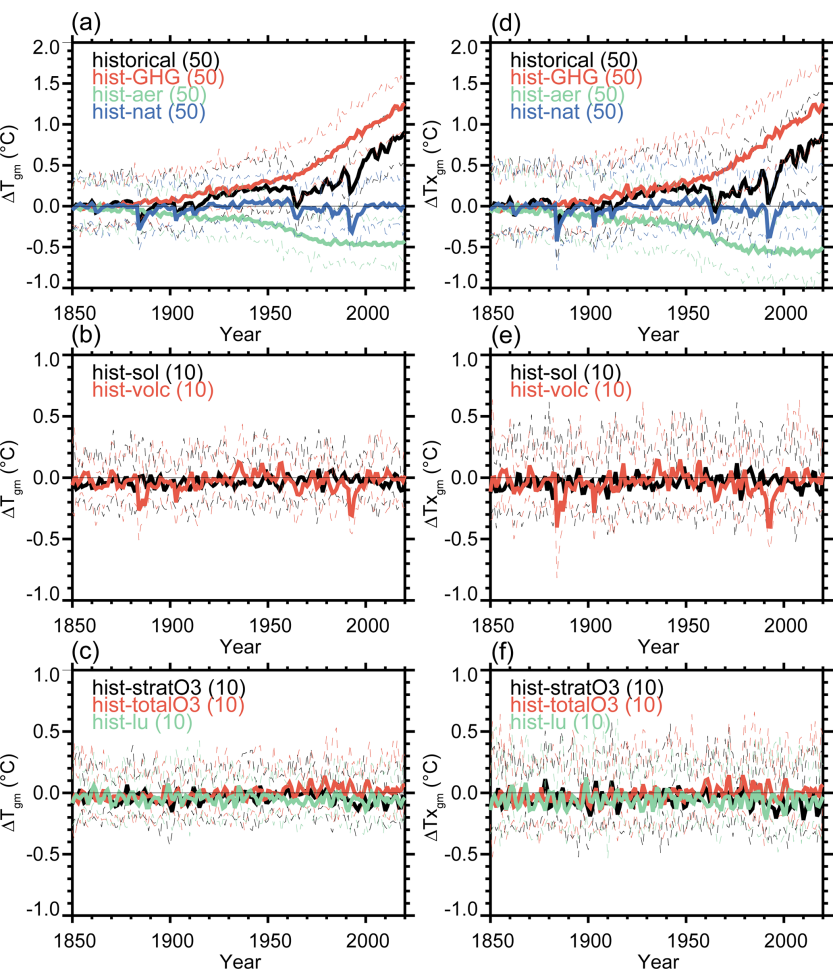
Figure 1. Changes in global mean T (**a–c**, °C) and T_x (**b–f**, °C) of historical all and single forcing experiments relative to the 1850–1900 averages of the ensemble-mean historical all forcing simulations. Solid lines are the ensemble means. Thin dashed lines denote the minimum and maximum values of the ensemble members. Numbers in parentheses indicate the ensemble sizes.

Table 3. List of future experiments.

Exp name	Forcing	Ens. size	Start year	End year	MIP (Tier)
ssp585	SSP5-8.5	50	2015	2100	ScenarioMIP (1)
ssp370	SSP3-7.0	50	2015	2100	ScenarioMIP (1)
ssp245	SSP2-4.5	50	2015	2100	ScenarioMIP (1)
ssp126	SSP1-2.6	50	2015	2100	ScenarioMIP (1)
ssp119	SSP1-1.9	50	2015	2100	ScenarioMIP (2)
ssp245-nat	Natural only of SSP2-4.5	50	2021	2100	DAMIP (3)
ssp245-GHG	GHG only of SSP2-4.5	50	2021	2100	DAMIP (2)
ssp245-aer	Anthropogenic aerosols only of SSP2-4.5	50	2021	2100	DAMIP (3)
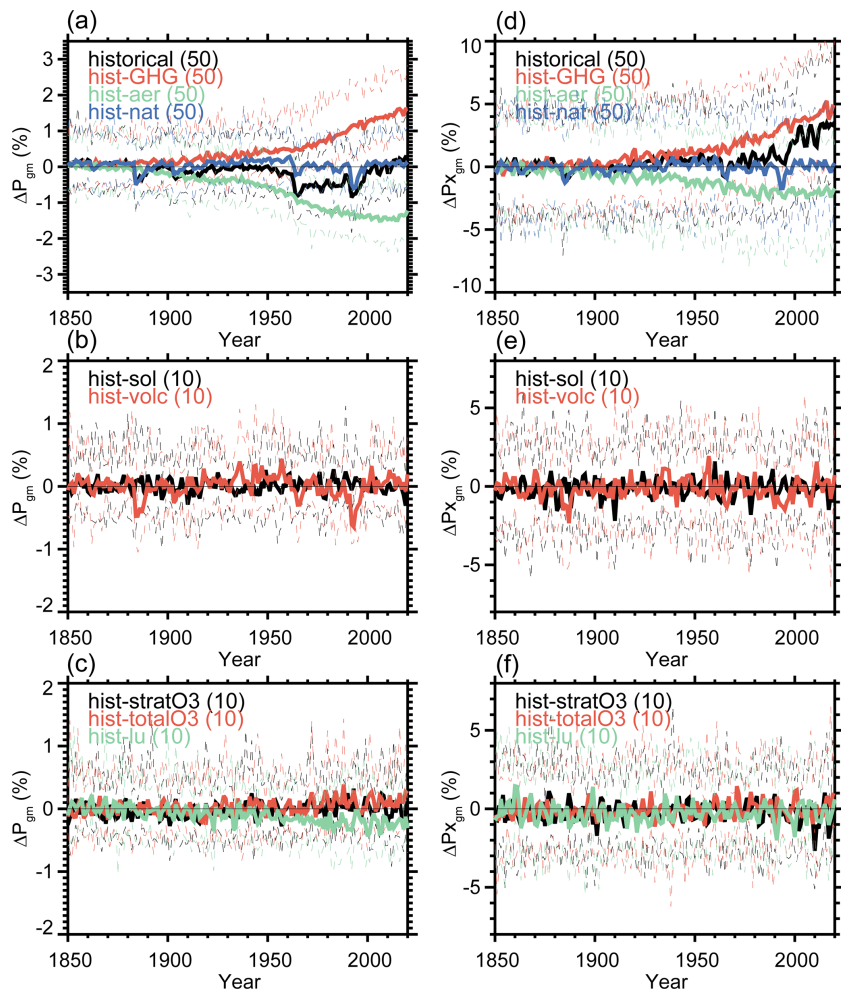
Figure 2. Global mean changes in P (**a–c**, %) and P_x (**d–f**, %) of historical all and single forcing experiments relative to the 1850–1900 averages of the ensemble-mean historical all forcing simulations. Solid lines are the ensemble means. Thin dashed lines denote the minimum and maximum values of the ensemble members. Numbers in parentheses indicate the ensemble sizes.

experiment), compute the ensemble averages for each experiment, and then calculate the sum of them. The min–max ranges of the sum of ensemble averaged single forcing runs (blue lines, hist-GHG + hist-aer + hist-totalO3 + hist-lu + hist-sol + hist-volc) overlap with the ranges of the ensemble averaged historical runs for all the regions and the

global mean for all four variables, suggesting that linear additivity holds for all of these cases, at least within MIROC6-LE.

Figure 4 shows differences in regional changes in T_x (2000–2020 minus 1850–1900) and P_x (percent changes from 1850–1900 to 2000–2020) between historical and hist-
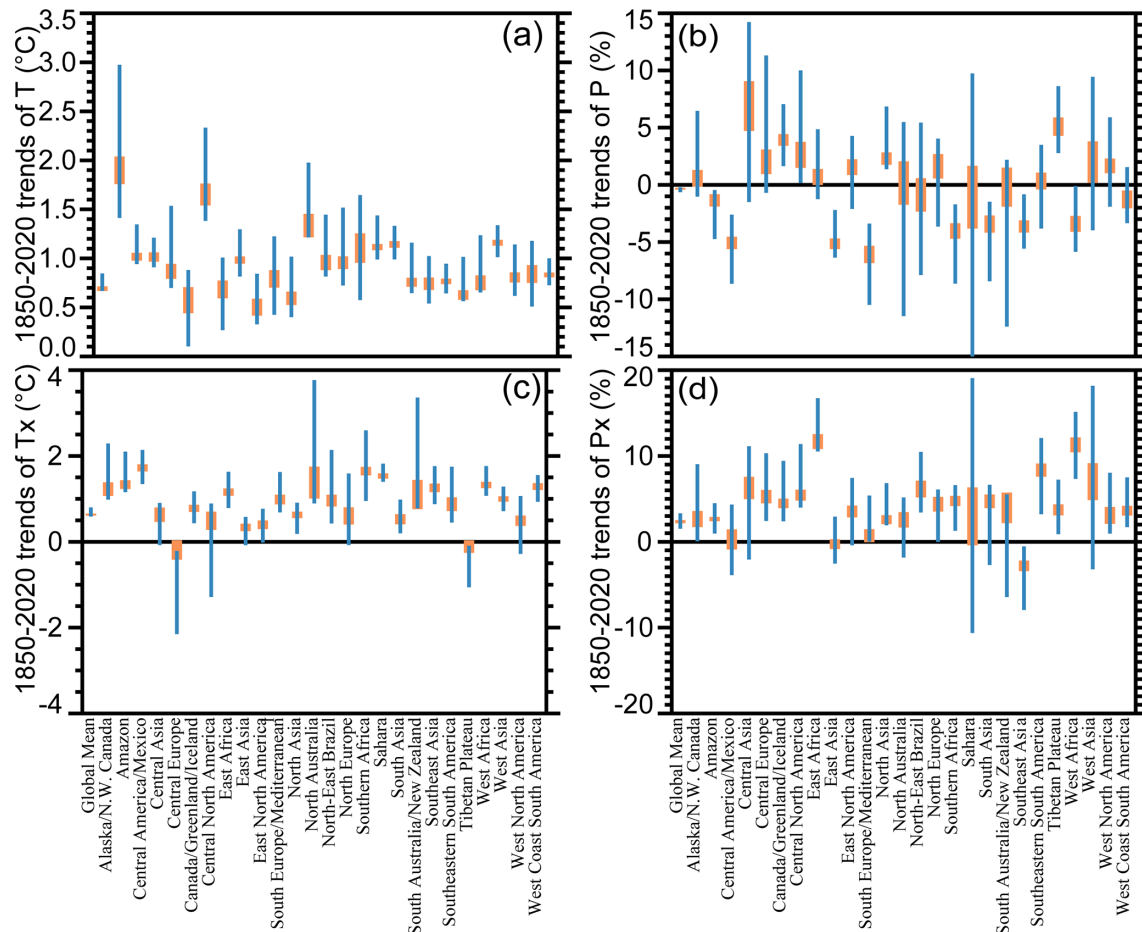
Figure 3. Additivity tests of historical experiments for the 1850–2020 trends of **(a)** T (°C), **(b)** P (%), **(c)** T_x (°C), and **(d)** P_x (%). These trends are calculated for the global mean or regional averages over the 26 regions defined by the IPCC (2012). Orange boxes indicate the min–max ranges of the 1000 ensemble average values for randomly sampled 50 member historical runs with replacement. Blue lines show the min–max ranges for 1000 sum values of ensemble averaged random samples from single forcing runs (hist-GHG + hist-aer + hist-totalO3 + hist-lu + hist-sol + hist-volc).

nat runs: these differences indicate anthropogenic influences on T_x and P_x changes. When we use only runs 1–3, anthropogenic signals of T_x are statistically significant at ±5 % levels of the t test over 73 % of the world but are not significant, for example, over the United States, Eastern Europe, and China. As the ensemble size (N) increases to $N = 10$ and 50, the fraction of the area where the anthropogenic T_x signals are significant rises to 90 % and 96 %, respectively. When we use only runs 1–3 or 1–10, the fraction of the area where anthropogenic P_x signals are significant are only 19 % and 35 %, respectively. Therefore, the ensemble sizes of $N = 3$ (the minimum size requested by DAMIP) or 10 (the minimum size requested by LESFMIP) are insufficient for isolating the historical anthropogenic changes in P_x over most of the world at the grid scale (150 km) using the single model ensemble. It should be noted that spatial aggregation or multimodel averages possibly improve signal-to-noise ratios.

Figure 5 shows the fractions of the world area (%) with significant differences (at ±5 % levels of the t test) between historical and hist-nat (i.e., anthropogenic signals) (F(historical, hist-nat)) as a function of ensemble size. As the ensemble size increases, F(historical, hist-nat) becomes larger. Area fractions are larger for temperature than for precipitation and greater for mean changes than for extremes. F(historical, hist-nat) are nearly saturated for $N = 4$ and 15 for T and T_x, respectively. In contrast, F(historical, hist-nat) is not saturated and rapidly increases with larger ensemble sizes for P and P_x. F(historical, hist-nat) of P and P_x reach 76 % and 69 % at $N = 50$, respectively. Therefore, an ensemble size of 50 is insufficient for isolating anthropogenic signals of P and P_x from the natural variability over 24 % and 31 % of the world's area (mainly in the subtropical ocean; Fig. 4f). In the rest of the world, anthropogenic signals of P and P_x are significant with the 50 member ensembles.
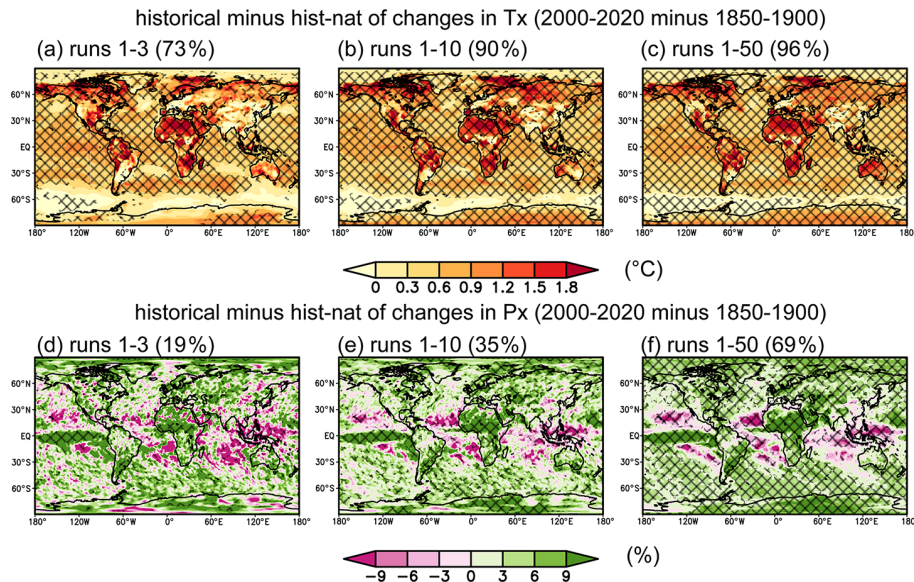
Figure 4. Panels **(a–c)** show the differences in changes in T_x (°C, 2000–2020 minus 1850–1900) between historical and hist-nat runs. Shading shows the ensemble mean of **(a)** runs 1–3, **(b)** runs 1–10, and **(c)** runs 1–50. Hatching denotes the regions where the differences are significant at 5 % levels of the t test. Parentheses indicate the fraction of the area with significant differences. Panels **(d–f)** show the same as the top panels but for differences in changes in P_x (percent changes of 2000–2020 relative to 1850–1900) between historical and hist-nat runs.

3.2   Future experiments

Single forcing experiments under the SSP2-4.5 scenario enable us to separate future climate responses to GHG, anthropogenic aerosols, and natural forcing factors (Fig. 6). For future simulations from 2015, volcanic forcing is increased from the value at the end of the historical simulation period (2015) over 10 years to the same constant value prescribed for the preindustrial control simulations and then is kept fixed (O'Neill et al., 2016). Although the future total solar irradiance is assumed to have a small negative long-term trend (Matthes et al., 2017), the effects on the long-term trends of T, T_x, P, and P_x are minimal. Positive responses of T, T_x, P, and P_x to the GHG forcing are partly compensated by the negative responses to the aerosol forcing. Because aerosol emissions gradually decrease under SSP2-4.5 (Rao, 2017; Lund, 2019), the negative responses of T, T_x, and P_x significantly decrease. Although negative responses of P to aerosol forcing also decrease, apparent differences of P changes between ssp245 and ssp245-GHG remain until 2100 mainly due to the large sensitivity of P to aerosol forcing (Shiogama et al., 2010a, b).

Figure 7 shows changes in global mean T, T_x, P and P_x under the five SSP scenarios. For T, T_x, and P_x, the differences between the scenarios are small until 2040, and after that, ssp runs with larger radiative forcing (ssp585 > ssp370 > ssp245 > ssp126 > ssp119) have greater positive anomalies. Changes in P are different from the other variables. At the end of the 21st century, the positive P anomalies from ssp370 are similar to those from ssp245, al-
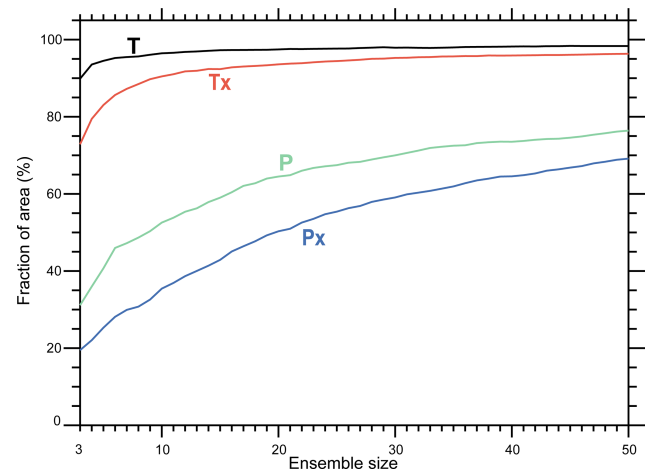

Figure 5. Fraction of the world area (%) with significant differences (at 5 % levels of the t test) between historical and hist-nat (2000–2020 minus 1850–1900) as a function of ensemble size.

though the T anomalies from ssp370 are larger than those from ssp245. Aerosol emissions do not decrease under the SSP3-7.0 scenario but decline in the other SSP scenarios (Rao, 2017; Lund, 2019). It is likely that greater negative responses of P to the larger aerosol emissions compensate substantially for the positive responses of P to the GHG forcing in ssp370. Differences in aerosol emissions between SSPs (O'Neil, 2014; Rao et al., 2017; Lund, 2019) also induce important differences in P anomalies until the middle of the
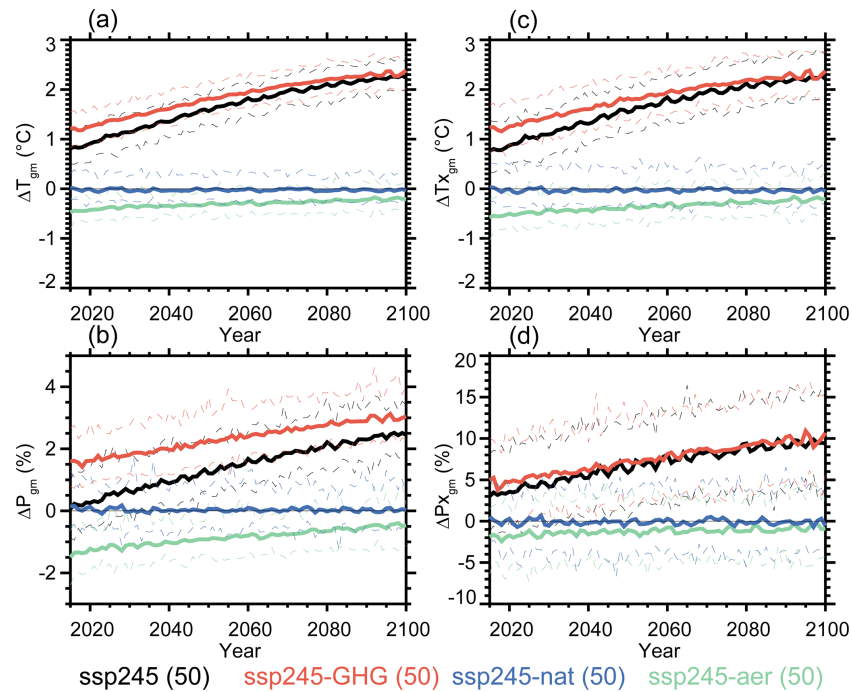
Figure 6. Future changes in global mean **(a)** T (°C), **(b)** P (%), **(c)** T_x (°C), and **(d)** P_x (%) relative to the 1850–1900 averages due to single forcing factors. Solid lines are the ensemble averages of ssp245 (black), ssp245-GHG (red), ssp245-aer (green), and ssp245-nat (blue). Thin dashed lines denote the minimum and maximum values of the ensemble members. Numbers in parentheses indicate the ensemble sizes.
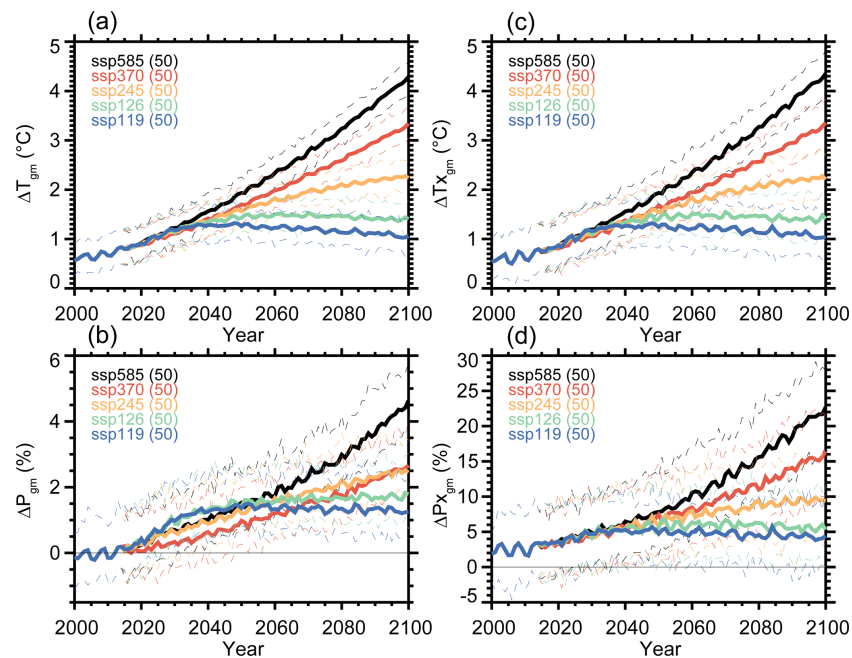

Figure 7. Future changes in global mean **(a)** T (°C), **(b)** P (%), **(c)** T_x (°C), and **(d)** P_x (%) relative to the 1850–1900 averages. Solid lines are the ensemble averages of ssp585 (black), ssp370 (red), ssp245 (orange), ssp126 (green), and ssp119 (blue). Thin dashed lines denote the minimum and maximum values of the ensemble members. Numbers in parentheses indicate the ensemble sizes.

21st century. It seems that rapid decreases in aerosol emissions due to aggressive reductions in fossil fuel consumption cause larger increases in P in ssp119 and ssp126 than in ssp585 (the fossil-fueled development scenario). The larger aerosol emissions in ssp370 (due to weak pollution control policies) would cause smaller increases in P in ssp370 than in the other ssp runs. Single forcing runs under all SSP scenarios (especially SSP3-7.0) would be useful for further analyses, but this remains the focus of future work.

The top panels of Fig. 8 show differences in changes in P_x (percent changes from 1850–1900 to 2050–2100) between ssp585 and ssp126. When we use only runs 1–3, differences in P_x are statistically significant over 49 % of the world's area but are not, for example, significant over the United States and Europe. As the ensemble size increases to 10 and 50, the fractions of areas with significant differences rise to 77 % and 90 %, respectively. When we analyze the differences in changes in P_x between ssp126 and ssp119 (the bottom panels of Fig. 8), only 38 % of the globe shows significant differences even when we have 50 member ensembles. When the ensemble size is limited to 10 or 3, the areas where differences are significant cover only 11 % and 7 %, respectively.

Figure 9 shows the fractions of areas with significant differences in T, T_x, P, and P_x changes (changes from 1850–1900 to 2050–2100) between the SSP experiments as a function of ensemble sizes (F(sspXXX, sspYYY)). It is expected that larger ensembles are necessary to identify differences in climate response for smaller differences of forcing. For T, F(ssp126, ssp119), F(ssp245, ssp126), F(ssp370, ssp126), and F(ssp585, ssp126) exceeded 80 %, even when only three members were available. For T_x, when F(ssp126, ssp119), F(ssp245, ssp126), F(ssp370, ssp126), and F(ssp585, ssp126) have 10 ensemble members, the areas are 84 %, 94 %, 97 %, and 99 %, respectively. Therefore, 10 members are sufficient to examine differences in T and T_x changes over most of the world. Fourteen and 13 members are necessary for F(ssp585, ssp126) of P and P_x to exceed 80 %, respectively. With $N = 25$, the F(ssp370, ssp126) of P and P_x reach 80 %. For the F(ssp245, ssp126) of P and P_x, $N \geq 38$ and 46 are necessary to exceed 70 %. The F(ssp126, ssp119) of P and P_x are less than 50 % for $N = 50$. Therefore, larger ensembles are desirable to investigate the differences in mean and extreme precipitation changes between ssp126 and ssp119, which were designed as experiments relevant to the 2 °C and 1.5 °C goals of the Paris Agreement (O'Neill et al., 2016).

3.3   Changes in internal variability

The internal variability in the historical (1951–2000) and future (2051–2100) experiments of MIROC6-LE are examined. Climate variability consists of externally forced change and internal variability, and isolating internal variability under transient forced changes with low errors requires large ensembles (Maher et al., 2018; Milinski et al., 2020; Lee et al., 2021) or spatiotemporal analysis methods (e.g., Wills et al., 2020). In this section, two conventional methods are compared for determining the internal variability component of an area-averaged variable: (1) a single-member-trend removed (SMTR) estimate using linearly detrended anomalies relative to the seasonal climatology over 50 years and (2) a multi-member-mean removed (MMMR) estimate using departures from the ensemble mean changing with time in response to external forcing. Hereafter, we represent the internal variability components of the first and second methods with "a" and "i": for instance, X_a and X_i for a variable X, respectively. While the first method is often used to analyze observational datasets and climate model outputs (e.g., Kim et al., 2014; Capotondi et al., 2020), the second method, which requires a large ensemble, is more appropriate for determining the internal variability component since it is not contaminated by residuals from detrending methods. The standard deviation is derived across time for each member and then averaged across ensemble members. We term the 50-member averages of the standard deviations derived by the MMMR estimate "the best estimate" in this study. As the reference state for the forced responses, the 800-year piControl is also analyzed, where X_i is the departure from the seasonal climatology over 800 years as the external forcing is constant for the year 1850, while the 50 members of X_a are derived from randomly selected 50-year segments. To focus on the interannual timescale, a 10-year high-pass Butterworth filter is applied.

The amplitude of the El Niño/Southern Oscillation (ENSO; Timmermann et al., 2018), the dominant interannual SST variability in the tropical Pacific Ocean, is examined based on the standard deviations of SSTa and SSTi averaged over the Niño-3.4 region (170–120° W, 5° S–5° N; Trenberth, 1997) in boreal winter (December to February). It has been reported that MIROC6 is one of the CMIP6 climate models that better simulates various key ENSO properties, such as spatial structure, global teleconnections, nonlinearity, and ENSO dynamics (Tatebe et al., 2019; Hayashi et al., 2020; Fasullo, 2020; Planton et al., 2021). In each MIROC6-LE experiment (Fig. 10a), the Niño-3.4 SSTa standard deviation varies among the ensemble members depending on the initial condition, but its 50-member ensemble average (shown with an open circle) approximates the best estimate (shown with a cross mark), implying that the forced response of the Niño-3.4 SST is not sensitive to interannual external forcing, such as volcanoes. Thus, the SMTR estimate can decompose the internal ENSO variability properly. Figure 10a also shows that the ENSO amplitude increases from the piControl to the historical (1951–2000) experiments and is further enhanced in all the future projections (ssp119, ssp126, ssp245, ssp370, and ssp585) for 2051–2100. The increased amplitude from the preindustrial condition of 1850 to 1951–2000 is consistent with the past ENSO changes inferred by McGregor et al. (2013). The future strengthening of ENSO SST variabil-
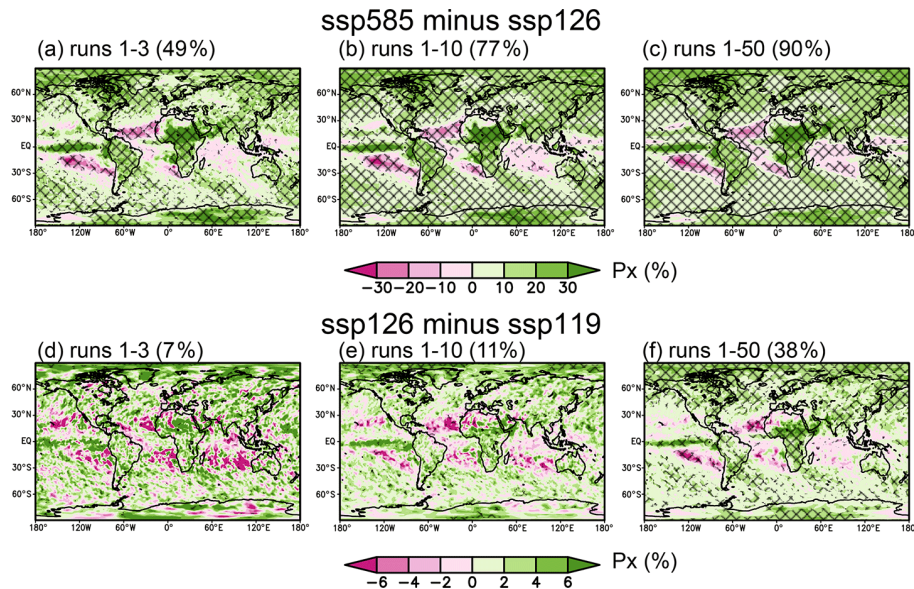
Figure 8. Panels **(a–c)** show the differences in changes in P_x (percent changes of 2050–2100 relative to 1850–1900) between ssp585 and ssp126 runs. Shading shows the ensemble mean of **(a)** runs 1–3, **(b)** runs 1–10, and **(c)** runs 1–50. Hatching denotes the regions where the differences are significant at 5 % levels of the t test. Numbers in parentheses indicate the fraction of the areas with significant differences. **(d–f)** The same as the top panels but for differences between ssp126 and ssp119.
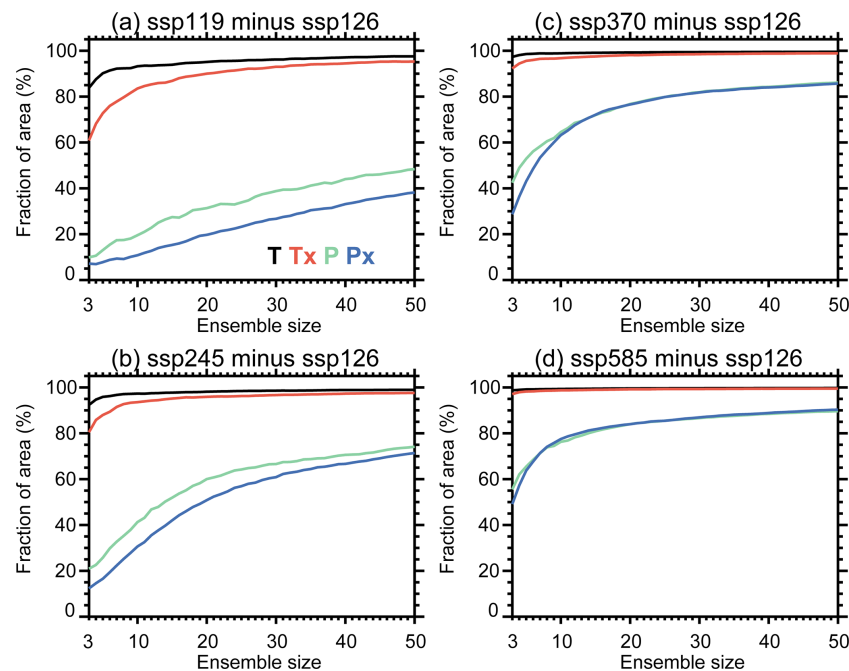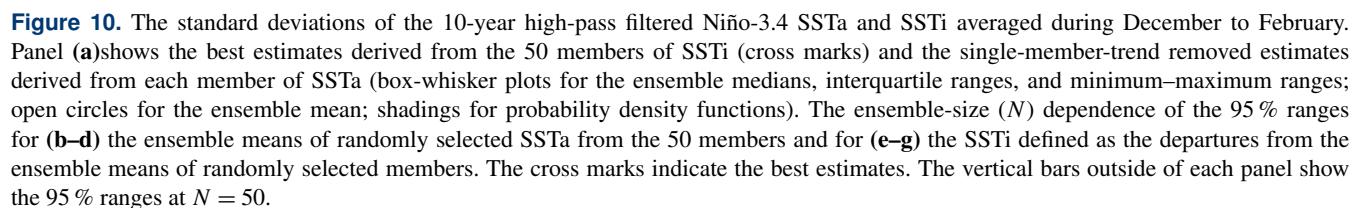

Figure 9. Fraction of the world area (%) with significant differences (at 5 % levels of the t test) between **(a)** ssp126 and ssp119, **(b)** ssp245 and ssp126, **(c)** ssp370 and ssp126, and **(d)** ssp585 and ssp126 as a function of ensemble size. Black, red, green, and blue lines are T, T_x, P, and P_x, respectively.

ity agrees with the majority of CMIP6 climate models under transient warming scenarios (Fredriksen et al., 2020; Cai et al., 2022), while equilibrated warmer climates may weaken ENSO (Callahan et al., 2021). The DAMIP experiments in-dicate that the increased GHG forcing contributes to ENSO amplification in the historical and ssp245 experiments, while the aerosol forcing also enhances ENSO in the historical ex-periment in MIROC6, as noted by Maher et al. (2023).

Figure 10. The standard deviations of the 10-year high-pass filtered Niño-3.4 SSTa and SSTi averaged during December to February. Panel **(a)** shows the best estimates derived from the 50 members of SSTi (cross marks) and the single-member-trend removed estimates derived from each member of SSTa (box-whisker plots for the ensemble medians, interquartile ranges, and minimum–maximum ranges; open circles for the ensemble mean; shadings for probability density functions). The ensemble-size (N) dependence of the 95 % ranges for **(b–d)** the ensemble means of randomly selected SSTa from the 50 members and for **(e–g)** the SSTi defined as the departures from the ensemble means of randomly selected members. The cross marks indicate the best estimates. The vertical bars outside of each panel show the 95 % ranges at $N = 50$.

How many ensemble members are needed for approximating the best estimate? In Fig. 10a, the 50-member ensemble averages (opened circles) correspond well to the best estimates (cross marks), but such a large ensemble requires significant computing resources and thus is not available for many climate models. To provide an efficient way to analyze internal variability in practice, the accuracy of ensemble averages with smaller ensemble sizes (e.g., 10 members) is evaluated. Here, the robustness of the ENSO amplitude

differences among the MIROC6-LE experiments is tested with respect to the ensemble size (N). The uncertainty in the SMTR estimate is shown in Fig. 10b–d, where the 95 % ranges between the 2.5th and 97.5th percentiles are calculated from 1000 pseudoensembles, which are produced for each N from 1 to 50 by resampling the 50 Niño-3.4 SSTa standard deviations randomly with replacement (Lee et al., 2021). The uncertainty range becomes larger with smaller values for N, and then two ranges in different experiments

may overlap at a specific small N, where the difference between two ensemble averages is possibly due to a lack of ensemble members. The minimum sizes of N needed for separating the two experiments beyond their 95 % ranges are summarized in Sect. S1 in the Supplement. To separate the historical from piControl experiments, $N = 3$ is at least required. The amplitude differences from historical to ssp370 and to ssp245 and ssp585 are detectable with $N \geq 3$ and $N \geq 4$, respectively, while much larger ensembles are required for ssp126 ($N \geq 20$) and ssp119 ($N \geq 33$). An ensemble with $N \geq 46$ can distinguish ssp370 from ssp245. However, the differences between ssp119 and ssp126, and among ssp245, ssp370, and ssp585, are not clearly obtained by $N = 50$; thus, a larger ensemble is required. In the DAMIP experiments, strengthening of ENSO from piControl can be detected with $N \geq 2$ for ssp245-GHG, $N \geq 7$ for hist-GHG, and $N \geq 23$ for hist-aer. The ENSO amplitude increase is also robustly detected from hist-GHG to the historical runs with $N \geq 22$ and from ssp245-GHG to ssp245 with $N \geq 37$, implying that external forcings other than GHG (e.g., aerosols) and the nonlinear relationship of forced responses may contribute to strengthening ENSO.

The ENSO amplitude uncertainty in the MMMR estimate with N is also shown in Fig. 10e–g, where the Niño-3.4 SSTi is defined as the departure from the ensemble mean of N members ($3 \leq N \leq 50$) randomly resampled with replacement. In general, a small N (e.g., $N = 3$) results in underestimating the internal variability amplitude, as the ensemble mean includes a higher residual variability (Milinski et al., 2020). For the ENSO amplitude, the results are basically the same as the SMTR estimate case (Fig. 10b–d), except for the detailed numbers. For example, $N \geq 5$ is required for separating historical runs from the piControl run, and $N = 8$ is large enough to detect the differences from historical runs to ssp245 ($N \geq 7$), ssp370 ($N \geq 6$), and ssp585 ($N \geq 8$). A larger N is required to identify differences among historical runs and ssp126 ($N \geq 19$) and ssp119 ($N \geq 31$). The ENSO strengthening from piControl to hist-GHG and hist-aer are detectable with $N \geq 8$ and $N \geq 27$, respectively. Importantly, a smaller ensemble size (e.g., $N = 10$) results in a higher probability of the underestimated standard deviation by the MMMR estimate, demonstrating the necessity of a large ensemble to evaluate the internal variability amplitude.

The internal variability in the global annual mean surface air temperature (T_a and T_i) and precipitation (P_a and P_i) shown in Sects. 3.1 and 3.2 are analyzed in the same manner as the ENSO amplitude. Figures 11a and 12a provide the amplitude dependence on the experiments. The variability is lower in the piControl experiment and higher in the high-emission scenarios (ssp245, ssp370, and ssp585). It also increases from piControl to hist-GHG and ssp245-GHG. Note that the SMTR estimates (Figs. 11b–d and 12b–d) overestimate the global mean T and P variabilities compared with the best estimates in the historical and hist-nat runs, in contrast to the ENSO amplitude. This is because the exter-

nally forced change at the interannual and decadal timescales driven by natural forcing, such as volcanic eruptions (Figs. 1a and 2a), cannot be separated from the internal variability and thus contaminates the T_a and P_a variabilities. Therefore, the MMMR estimate (T_i and P_i) is necessary for distinguishing the internal variability components from the forced responses in the global mean T and P of the historical and hist-nat experiments (Figs. 11e–g and 12e–g).

Based on the MMMR estimate, the minimum ensemble size for detecting the increase in the global mean T_i standard deviation is $N = 6$ for the piControl to historical runs, $N = 7$ for the historical to ssp370 runs, $N = 8$ for the historical to ssp245 and ssp585 runs, and $N = 23$ for the historical to ssp119 and ssp126 runs. The differences between ssp119 and ssp126, and among ssp245, ssp370, and ssp585, are not significant even for $N = 50$. Interestingly, the global mean T_i standard deviations tend to be higher in ssp370 than in ssp585, similarly to ENSO, indicating the critical role of ENSO variability on the global mean air temperature variance (e.g., Thompson et al., 2009; Hu and Fedorov, 2017). In contrast, the global mean P_i standard deviations overlap with each other for about 95 % of their ranges such that the differences among historical, ssp119, and ssp126 runs are not robust even for $N = 50$. However, when $N \geq 16$ is greater than or equal to 16, the increase is significant from historical scenarios to the high-emission scenarios (ssp245, ssp370, and ssp585), for $N = 50$ from ssp126 to ssp245, and for $N = 47$ and 33 for ssp245 to ssp370 and ssp585, respectively. Unlike the global mean T_i and ENSO variabilities, the P_i variability is higher in ssp370 and ssp585 than in ssp245. It is significant for $N \geq 10$ that the increased variability in both the global mean T_i and P_i is driven by GHG (hist-GHG and ssp245-GHG), but the amplitudes of that variability in the other DAMIP experiments remain indistinguishable in the piControl run, even with $N = 50$. Thus, a larger ensemble and longer piControl simulation are desirable for detecting changes in the global mean T and P internal variability amplitude from the piControl to hist-aer, hist-nat, ssp245-aer, and ssp245-nat simulations.

In summary, MIROC6-LE with $N = 50$ is useful for detecting changes in the internal variability of ENSO and global mean T and P anomalies between historical and future experiments and between high- and low-emission scenarios. The impact of aerosols on ENSO amplitude is also detectable in MIROC6. However, it is still challenging to distinguish these changes between high-emission scenarios or between low-emission scenarios, implying the importance of implementing spatiotemporal analysis methods (e.g., Wills et al., 2020) or generating larger ensembles (e.g., Maher et al., 2019; Rodgers et al., 2021; Lin et al., 2022). The mechanisms underlying the clearly detected changes in this study and the changes in other internal variability will be reported in future works.
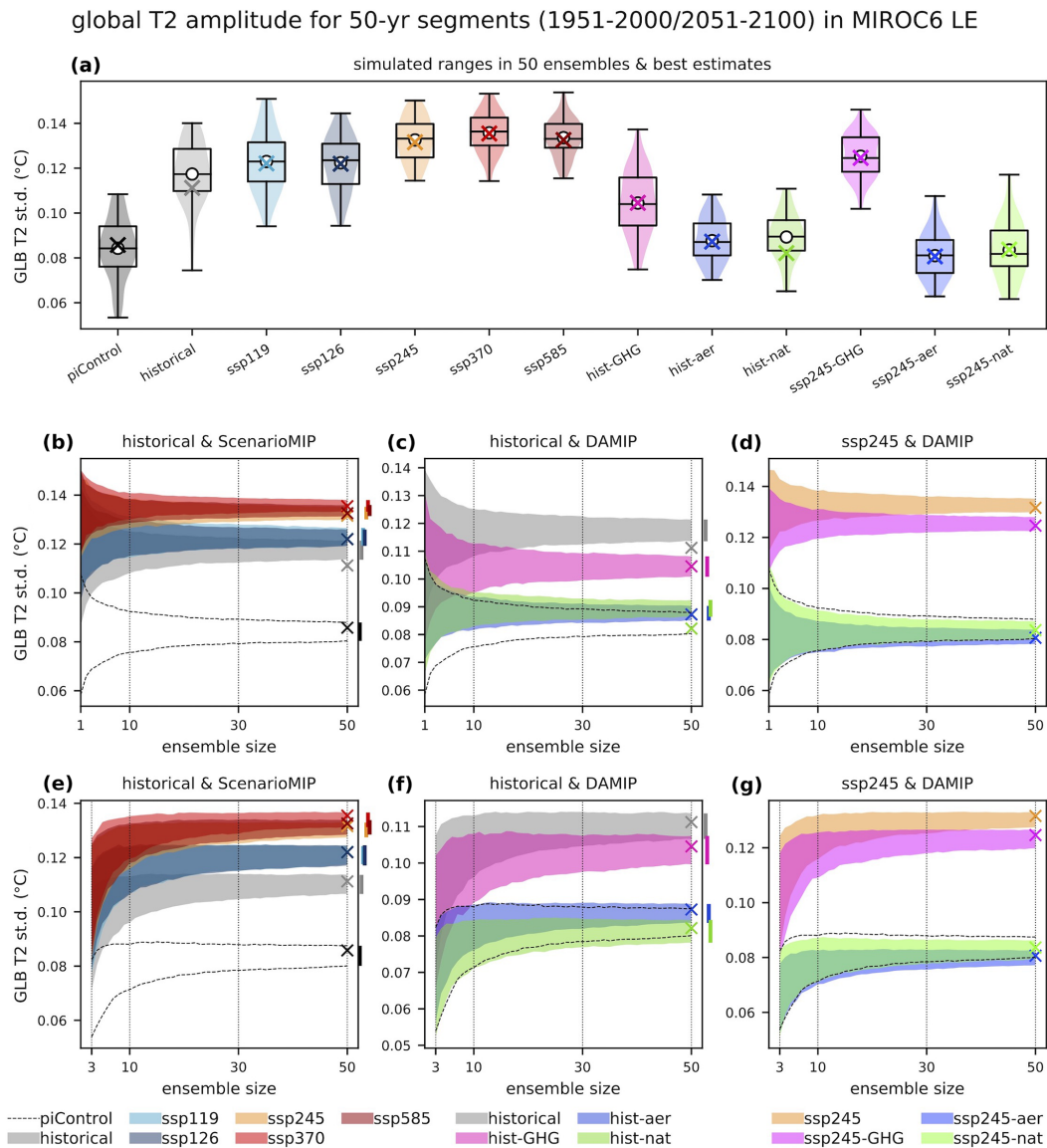
global T2 amplitude for 50-yr segments (1951-2000/2051-2100) in MIROC6 LE

Figure 11. Same as Fig. 10 but for the 10-year high-pass-filtered global annual mean T (°C).

4 Discussion and conclusion

Here, we have explained how MIROC6-LE was designed. We have also shown the results of the initial analyses. Specifically, we find that the linear additivity of the forcing-response relationship holds for the 1850–2020 trends of T, T_x, P, and P_x by analyzing the historical all forcing runs and the sum of single forcing historical runs. The ensemble sizes of 4 and 15 are enough to isolate historical anthropogenic signals (differences between historical and hist-nat runs) of T and T_x in most of the world. Although historical anthropogenic signals of P and P_x are significant with the 50-member ensembles in approximately 70 % of the world, larger ensembles are necessary in other areas (mainly in the subtropics). The 50-member simulations of MIROC6-

LE are sufficient to analyze differences in regional T and T_x changes between ssp126 and ssp119 (scenarios relevant to the 2 °C and 1.5 °C goals of the Paris Agreement) but not sufficient to obtain significant differences in P and P_x changes over more than half of the world. Atmospheric global climate models (AGCMs) are more cost-effective tools to produce large ensembles (e.g., 100 members) for future climate change projections at given warming levels and for event attribution studies than CGCMs, while AGCM simulations can only inform projections and attribution statements conditionally with respect to prescribed SST patterns (Shiogama et al., 2016, 2020; Mizuta et al., 2017; Mitchell et al., 2017; Imada et al., 2017; Stone et al., 2019; Fujita et al., 2020; Nosaka et al., 2021). Combined analyses of AGCM LEs (e.g., Mitchell et al., 2017; Shiogama et al., 2019b) and
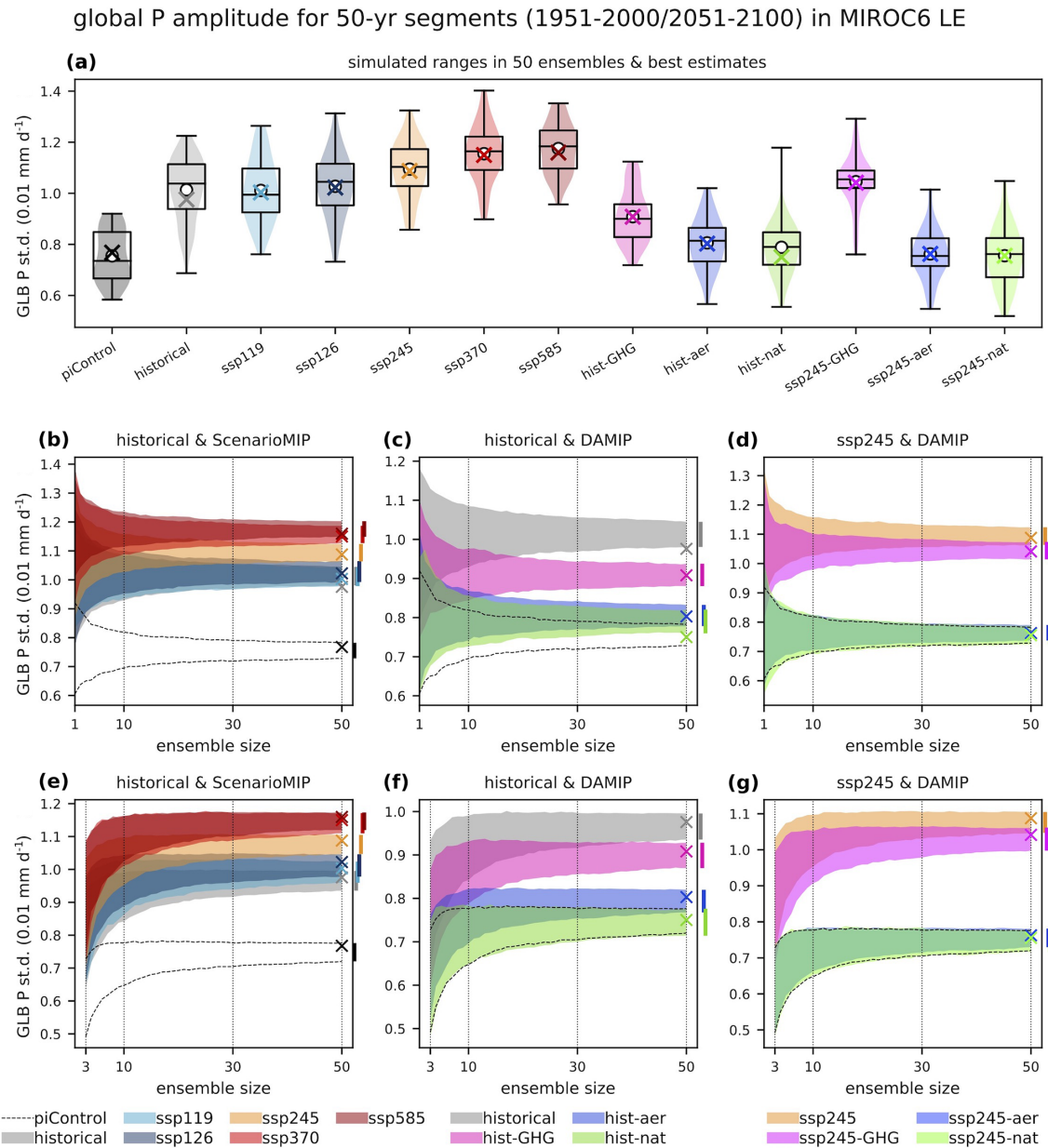
global P amplitude for 50-yr segments (1951-2000/2051-2100) in MIROC6 LE

Figure 12. Same as Fig. 10 but for the 10-year high-pass-filtered global annual mean P $(0.01\,\mathrm{mm\,d^{-1}})$.

CGCM LEs could be useful for discussions of differences in precipitation changes between the 2 °C and 1.5 °C warmer climates, but it should be noted that climate change projections can be significantly different between AGCM and CGCM simulations (Uhe et al., 2021).

We also analyzed the historical and future changes in ENSO variability and the internal components of interannual global mean T and P variabilities using MIROC6-LE. The interannual variabilities are the 10-year high-pass-filtered components of departures from the ensemble mean so that interannual and decadal responses to the natural forcing can be eliminated, and they are compared with detrended

anomalies relative to the long-term mean. The future ENSO intensification over the 50-year window of 2051–2100 is detectable with ensemble sizes of 6 for ssp370 (minimum of the five scenarios examined) and 31 for ssp119 (maximum), and the ensemble size of 27 can isolate the contributions of the historical GHG and aerosol forcings to the ENSO intensification during the historical period. For detecting the future amplification in the interannual T variability, the ensemble sizes of 8 and 23 are sufficient in the high-emission scenarios (ssp245, ssp370, and ssp585) and in the low-emission scenarios (ssp119 and ssp126), respectively, but the differences between the low- and high-emission scenarios cannot

be isolated even with 50 members. As these unforced global mean T variability changes basically follow the ENSO amplitude changes (cf. Thompson et al., 2009), a better understanding of ENSO projections is key for reducing the uncertainty of global temperature projections. The P variability amplification from the historical runs can be detected in the high-emission scenarios with 16 members, but 50 members are not sufficient in the low-emission scenarios. It is worth noting that a large ensemble is necessary to avoid underestimating the amplitude of internal variability relative to the ensemble mean. Furthermore, the historical natural forcing results in an overestimation of the global mean T and P variabilities for interannual timescales when the detrended anomalies are used, highlighting the importance of using the departures from the ensemble mean for discussing changes in the internal variability.

MIROC6-LE is one of the largest LEs to date. The total simulation length of MIROC6-LE is 76 750 years, which is much larger than that of other LEs, e.g., CESM2-LE (32 675 years), MPI-GE (58 800 years), and SMHI-LENS (19 450 years), and is comparable to the DAMIP experiments of CanESM5 (72 515 years, https://pcmdi.llnl.gov/CMIP6/ArchiveStatistics/esgf_data_holdings/DAMIP/index.html, last access: 13 October 2023). Because MIROC6-LE is an evolving ensemble, additional experiments will be included in the future. We are publishing the output data of MIROC6-LE via the Earth System Grid Federation. When this paper was submitted, the output data of all the experiments, except for runs 1–10 of hist-lu and runs 11–50 of hist-aer and ssp245-aer, had been published. Because the experimental designs of MIROC6-LE are consistent with those of the other MIPs, it is easy to compare the outputs of MIROC6-LE with the other models. We hope that the publicly available output data of MIROC6-LE facilitate research in a broad range of communities.

References

Cai, W., Ng, B., Wang, G., Santoso, A., Wu, L., and Yang, K.: Increased ENSO sea surface temperature variability under four IPCC emission scenarios, Nat. Clim. Chang. 12, 228–231, https://doi.org/10.1038/s41558-022-01282-z, 2022.

Capotondi, A., Wittenberg, A. T., Kug, J.-S., Takahashi, K., and McPhaden, M. J.: ENSO Diversity, in: El Niño Southern Oscillation in a Changing Climate, edited by: McPhaden, M. J., Santoso, A., and Cai, W., https://doi.org/10.1002/9781119548164.ch4, 2020.

Callahan, C. W., Chen, C., Rugenstein, M., Bloch-Johnson, J., Yang S., and Moyer, E. J.: Robust decrease in El Niño-/Southern Oscillation amplitude under long-term warming, Nat. Clim. Change, 11, 752–757, https://doi.org/10.1038/s41558-021-01099-2, 2021.

Deser, C., Phillips, A. S., Simpson, I. R., Rosenbloom, N., Coleman, D., Lehner, F., Pendergrass, A., DiNezio, P., and Stevenson, S.: Isolating the Evolving Contributions of Anthropogenic Aerosols and Greenhouse Gases: A New CESM1 Large Ensemble Community Resource, J. Climate, 33, 7835–7858, https://doi.org/10.1175/JCLI-D-20-0123.1, 2020.

Devaraju, N., Bala, G., and Modak, A.: Effects of large-scale deforestation on precipitation in the monsoon regions: Remote versus local effects, P. Natl. Acad. Sci. USA, 112, 3257–3262, https://doi.org/10.1073/pnas.1423439112, 2015.

Eyring, V., Bony, S., Meehl, G. A., Senior, C. A., Stevens, B., Stouffer, R. J., and Taylor, K. E.: Overview of the Coupled Model Intercomparison Project Phase 6 (CMIP6) experimental design and organization, Geosci. Model Dev., 9, 1937–1958, https://doi.org/10.5194/gmd-9-1937-2016, 2016.

Fasullo, J. T.: Evaluating simulated climate patterns from the CMIP archives using satellite and reanalysis datasets using the Climate Model Assessment Tool (CMATv1), Geosci. Model Dev., 13, 3627–3642, https://doi.org/10.5194/gmd-13-3627-2020, 2020.

Fredriksen, H.-B., Berner, J., Subramanian, A. C., and Capotondi, A.: How does El Niño–Southern Oscillation change under global warming – A first look at CMIP6, Geophys. Res. Lett., 47, e2020GL090640, https://doi.org/10.1029/2020GL090640, 2020.

Fujita, M., Mizuta, R., Ishii, M., Endo, H., Sato, T., Okada, Y., Kawazoe, S., Sugimoto, S., Ishihara, K., and Watanabe, S.: Precipitation Changes in a Climate With 2 K Surface Warming From Large Ensemble Simulations Using 60 km Global and 20 km Regional Atmospheric Models, Geophys. Res. Lett., 46, 435–442, 2020.

Gillett, N. P., Shiogama, H., Funke, B., Hegerl, G., Knutti, R., Matthes, K., Santer, B. D., Stone, D., and Tebaldi, C.: The Detection and Attribution Model Intercomparison Project (DAMIP v1.0) contribution to CMIP6, Geosci. Model Dev., 9, 3685–3697, https://doi.org/10.5194/gmd-9-3685-2016, 2016.

Gillett, N. P., Kirchmeier-Young, M., Ribes, A., Shiogama, H., Hegerl, G., Knutti, R., Gastineau, G., John, J. G., Li, L., Nazarenko, L., Rosenbloom, N., Seland, Ø., Wu, T., Yukimoto, S., and Ziehn, T.: Constraining human contributions to observed warming since the pre-industrial period, Nat. Clim. Change, 11, 207–212 https://doi.org/10.1038/s41558-020-00965-9, 2021.

Iles, C. E. and Hegerl, G. C.: The global precipitation response to volcanic eruptions in the CMIP5 models, Environ. Res. Lett., 9, 104012, https://doi.org/10.1088/1748-9326/9/10/104012, 2014.

Imada, Y., Maeda, S., Watanabe, M., Shiogama, H., Mizuta, R., Ishii, M., and Kimoto, M.: Recent enhanced seasonal temperature contrast in Japan from large ensemble high-resolution climate simulations, Atmosphere, 8, 57, https://doi.org/10.3390/atmos8030057, 2017.

Intergovernmental Panel on Climate Change (IPCC): Managing the Risks of Extreme Events and Disasters to Advance Climate Change Adaptation, in: A Special Report of Working Groups I and II of the Intergovernmental Panel on Climate Change, edited by: Field, C. B., Barros, V., Stocker, T. F., Qin, D., Dokken, D. J., Ebi, K. L., Mastrandrea, M. D., Mach, K. J., Plattner, G.-K., Allen, S. K., Tignor, M., and Midgley, P. M., Cambridge University Press, Cambridge, United Kingdom and New York, NY, USA, 582 pp., 2012.

Hayashi, M., Jin, F. F., and Stuecker, M. F: Dynamics for El Niño-La Niña asymmetry constrain equatorial-Pacific warming pattern, Nat. Commun., 11, 4230, https://doi.org/10.1038/s41467-020-17983-y, 2020.

Hawkins, E. and Sutton, R. T.: The potential to narrow uncertainty in projections of regional precipitation change, Clim. Dynam., 37, 407–418, https://doi.org/10.1007/s00382-010-0810-6, 2011.

Hu, S. and Fedorov, A. V.: The extreme El Niño of 2015–2016 and the end of global warming hiatus, Geophys. Res. Lett., 44, 3816–3824, https://doi.org/10.1002/2017GL072908, 2017.

Kay, J. E., Deser, C., Phillips, A., Mai, A., Hannay, C., Strand, G., Arblaster, J., Bates, S., Danabasoglu, G., Edwards, J., Holland, M. Kushner, P., Lamarque, J.-F., Lawrence, D., Lindsay, K., Middleton, A., Munoz, E., Neale, R., Oleson, K., Polvani, L., and Vertenstein, M.: The Community Earth System Model (CESM) Large Ensemble Project: A Community Resource for Studying Climate Change in the Presence of Internal Climate Variability, B. Am. Meteorol. Soc., 96, 1333–1349, https://doi.org/10.1175/BAMS-D-13-00255.1, 2015.

Kim, S., Cai, W., Jin, F. F., Santoso, A., Wu, L., Guilyardi, E., and An, S.: Response of El Niño sea surface temperature variability to greenhouse warming, Nat. Clim. Change, 4, 786–790, https://doi.org/10.1038/nclimate2326, 2014.

Lee, J., Planton, Y. Y., Gleckler, P. J., Sperber, K. R., Guilyardi, E., Wittenberg, A. T., McPhaden, M. J., and Pallotta, G.: Robust evaluation of ENSO in climate models: How many ensemble members are needed?, Geophys. Res. Lett., 48, e2021GL095041, https://doi. org/10.1029/2021GL095041, 2021.

Lehner, F., Deser, C., Maher, N., Marotzke, J., Fischer, E. M., Brunner, L., Knutti, R., and Hawkins, E.: Partitioning climate projection uncertainty with multiple large ensembles and CMIP5/6, Earth Syst. Dynam., 11, 491–508, https://doi.org/10.5194/esd-11-491-2020, 2020.

Lin, P., Zhao, B., Wei, J., Liu, H., Zhang, W., Chen, X., Jiang, J., Ding, M., Man, W., Jiang, J., Zhang, X., Ding, Y., Bai, W., Jin, C., Yu, Z., Li, Y., Zheng, W., and Zhou, T.: The Super-large Ensemble Experiments of CAS FGOALS-g3, Adv. Atmos. Sci. 39, 1746–1765, https://doi.org/10.1007/s00376-022-1439-1, 2022.

Lund, M. T., Myhre, G., and Samset, B. H.: Anthropogenic aerosol forcing under the Shared Socioeconomic Pathways, Atmos. Chem. Phys., 19, 13827–13839, https://doi.org/10.5194/acp-19-13827-2019, 2019.

Maher, N., Matei, D., Milinski, S., and Marotzke, J.: ENSO change in climate projections: Forced response or internal variability?, Geophys. Res. Lett., 45, 11390–11398, https://doi.org/10.1029/2018GL079764, 2018.

Maher, N., Milinski, S., Suarez-Gutierrez, L., Botzet, M., Dobrynin, M., Kornblueh, L., Kröger, J., Takano, Y., Ghosh, R., Hedemann, C., Li, C., Li, H., Manzini, E., Notz, N., Putrasahan, D., Boysen, L., Claussen, M., Ilyina, T., Olonscheck, D., Raddatz, T., Stevens, B., and Marotzke, J.: The Max Planck Institute Grand Ensemble: Enabling the Exploration of Climate System Variability, J. Adv. Model. Earth Sy., 11, 1–21, https://doi.org/10.1029/2019MS001639, 2019.

Maher, N., Wills, R. C. J., DiNezio, P., Klavans, J., Milinski, S., Sanchez, S. C., Stevenson, S., Stuecker, M. F., and Wu, X.: The future of the El Niño–Southern Oscillation: using large ensembles to illuminate time-varying responses and inter-model differences, Earth Syst. Dynam., 14, 413–431, https://doi.org/10.5194/esd-14-413-2023, 2023.

Matthes, K., Funke, B., Andersson, M. E., Barnard, L., Beer, J., Charbonneau, P., Clilverd, M. A., Dudok de Wit, T., Haberreiter, M., Hendry, A., Jackman, C. H., Kretzschmar, M., Kruschke, T., Kunze, M., Langematz, U., Marsh, D. R., Maycock, A. C., Misios, S., Rodger, C. J., Scaife, A. A., Seppälä, A., Shangguan, M., Sinnhuber, M., Tourpali, K., Usoskin, I.,

van de Kamp, M., Verronen, P. T., and Versick, S.: Solar forcing for CMIP6 (v3.2), Geosci. Model Dev., 10, 2247–2302, https://doi.org/10.5194/gmd-10-2247-2017, 2017.

McGregor, S., Timmermann, A., England, M. H., Elison Timm, O., and Wittenberg, A. T.: Inferred changes in El Niño–Southern Oscillation variance over the past six centuries, Clim. Past, 9, 2269–2284, https://doi.org/10.5194/cp-9-2269-2013, 2013.

Milinski, S., Maher, N., and Olonscheck, D.: How large does a large ensemble need to be?, Earth Syst. Dynam., 11, 885–901, https://doi.org/10.5194/esd-11-885-2020, 2020.

Mitchell, D., AchutaRao, K., Allen, M., Bethke, I., Beyerle, U., Ciavarella, A., Forster, P. M., Fuglestvedt, J., Gillett, N., Haustein, K., Ingram, W., Iversen, T., Kharin, V., Klingaman, N., Massey, N., Fischer, E., Schleussner, C.-F., Scinocca, J., Seland, Ø., Shiogama, H., Shuckburgh, E., Sparrow, S., Stone, D., Uhe, P., Wallom, D., Wehner, M., and Zaaboul, R.: Half a degree additional warming, prognosis and projected impacts (HAPPI): background and experimental design, Geosci. Model Dev., 10, 571–583, https://doi.org/10.5194/gmd-10-571-2017, 2017.

Mizuta A. O., Imad, R., Murata, A., Ishii, M., Shiogama, H., Hibino, K., Mori, N., a, Y., Yoshida, K., Aoyagi, T., Kawase, H., Mori, M., Okada, Y., Shimura, T., Nagatomo, T., Ikeda, M., Endo, H., Nosaka, M., Arai, M., Takahashi, C., Tanaka, K., Takemi, T., Tachikawa, Y., Temur, K., Kamae, Y., Watanabe, M., Sasaki, H., Kitoh, A., Takayabu, I., Nakakita, E., and Kimoto, M.: Over 5000 years of ensemble future climate simulations by 60 km global and 20 km regional atmospheric models, B. Am. Meteor. Soc., 98, 1383–1398, https://doi.org/10.1175/BAMS-D-16-0099.1., 2017.

Nosaka, M., Ishii, M., Shiogama, H., Mizuta, R., Murata, A., Kawase, H., and Sasaki, H.: Scalability of future climate changes across Japan examined with large-ensemble simulations at +1.5 K, +2 K, and +4 K global warming levels, Prog. Earth Planet. Sci., 7, https://doi.org/10.1186/s40645-020-00341-3, 2020.

O'Neill, B. C., Kriegler, E., Riahi, K., Ebi, K. L., Hallegatte, S., Carter, T. R., Mathur, R., and van Vuuren, D. P.: A new scenario framework for climate change research: the concept of shared socioeconomic pathways, Clim. Change, 122, 387–400, 2014.

O'Neill, B. C., Tebaldi, C., van Vuuren, D. P., Eyring, V., Friedlingstein, P., Hurtt, G., Knutti, R., Kriegler, E., Lamarque, J.-F., Lowe, J., Meehl, G. A., Moss, R., Riahi, K., and Sanderson, B. M.: The Scenario Model Intercomparison Project (ScenarioMIP) for CMIP6, Geosci. Model Dev., 9, 3461–3482, https://doi.org/10.5194/gmd-9-3461-2016, 2016.

Planton, Y. Y., Guilyardi, E., Wittenberg, A. T., Lee, J., Gleckler, P. J., Bayr, T., McGregor, S., McPhaden, M. J., Power, S., Roehrig, R., Vialard, J., and Voldoire, A.: Evaluating Climate Models with the CLIVAR 2020 ENSO Metrics Package, B. Am. Meteorol. Soc., 102, 193–217, https://doi.org/10.1175/BAMS-D-19-0337.1, 2021.

Rao, S., Klimont Z., Smith, S. J., Van Dingenen, R., Dentener, F., Bouwman, L., Riahi, K., Mann, M., Leon Bodirsky, B., van Vuuren, D. P., Reis, L. A., Calvin, K., Drouet, L., Fricko, O., Fujimori, S., Gernaat, D., Havlik, P., Harmsen, M., Hasegawa, T., Heyes, C., Hilaire, J., Luderer, G., Masui, T., Stehfest, E., Strefler, J., van der Sluis, S., and Tavoni, M.: Future air pollution in the Shared Socio-economic Pathways, Glob. Environ. Change,

42, 346–358, https://doi.org/10.1016/j.gloenvcha.2016.05.012, 2017.

Rodgers, K. B., Lee, S.-S., Rosenbloom, N., Timmermann, A., Danabasoglu, G., Deser, C., Edwards, J., Kim, J.-E., Simpson, I. R., Stein, K., Stuecker, M. F., Yamaguchi, R., Bódai, T., Chung, E.-S., Huang, L., Kim, W. M., Lamarque, J.-F., Lombardozzi, D. L., Wieder, W. R., and Yeager, S. G.: Ubiquity of human-induced changes in climate variability, Earth Syst. Dynam., 12, 1393–1411, https://doi.org/10.5194/esd-12-1393-2021, 2021.

Shiogama, H.: MIROC MIROC6 model output prepared for CMIP6 DAMIP, Version 20230414, Earth System Grid Federation, [data set], https://doi.org/10.22033/ESGF/CMIP6.894, 2019.

Shiogama, H., Emori, S., Takahashi, K., Nagashima, T., Ogura, T., Nozawa, T., and Takemura, T.: Emission scenario dependency of precipitation on global warming in the MIROC3.2 model, J. Climate, 23, 2404–2417, 2010a.

Shiogama, H., Hanasaki, N., Masutomi, Y., Nagashima, T., Ogura, T., Takahashi, K., Hijioka, Y., Takemura, T., Nozawa, T., and Emori, S.: Emission scenario dependencies in climate change assessments of the hydrological cycle, Clim. Change, 99, 321–329, https://doi.org/10.1007/s10584-009-9765-1, 2010b.

Shiogama, H., Stone, D. A., Nagashima, T., Nozawa, T., and Emori, S.: On the linear additivity of climate forcing-response relationships at global and continental scales, Int. J. Clim., 33, 2542–2550, https://doi.org/10.1002/joc.3607, 2013.

Shiogama, H., Imada, Y., Mori, M., Mizuta, R., Stone, D., Yoshida, K., Arakawa, O., Ikeda, M., Takahashi, C., Arai, M., Ishii, M., Watanabe, M. M., and Kimoto, M.: Attributing historical changes in probabilities of record-breaking daily temperature and precipitation extreme events, SOLA, 12, 225–231, 2016.

Shiogama, H., Abe, M., and Tatebe, H.: MIROC MIROC6 model output prepared for CMIP6 ScenarioMIP. Version 20230414, Earth System Grid Federation, [data set], https://doi.org/10.22033/ESGF/CMIP6.898, 2019a.

Shiogama, H., Hasegawa, T., Fujimori, S., Murakami, D., Takahashi, K., Tanaka, K., Emori, S., Kubota, I., Abe, M., Imada, Y., Watanabe, M., Mitchell, D., Schaller, N., Sillmann, J., Fischer, E., Scinocca, J. F., Bethke, I., Lierhammer, L., Takakura, J., Trautmann, T., Döll, P., Ostberg, S., Schmied, H. M., Saeed, F., and Schleussner, C.-F.: Limiting global warming to 1.5 °C will lower increases in inequalities of four hazard indicators of climate change, Environ. Res. Lett., 14, 124022, https://doi.org/10.1088/1748-9326/ab5256, 2019b.

Shiogama, H., Hirata, R., Hasegawa, T., Fujimori, S., Ishizaki, N. N., Chatani, S., Watanabe, M., Mitchell, D., and Lo, Y. T. E.: Historical and future anthropogenic warming effects on droughts, fires and fire emissions of CO_2 and $PM_{2.5}$ in equatorial Asia when 2015-like El Niño events occur, Earth Syst. Dynam., 11, 435–445, https://doi.org/10.5194/esd-11-435-2020, 2020.

Shiogama, H., Watanabe, M., Kim, H., and Hirota, N.: Emergent constraints on future precipitation changes, Nature, 602, 612–616, https://doi.org/10.1038/s41586-021-04310-8, 2022.

Stone, D. A., Christidis, N., Folland, C., Perkins-Kirkpatrick, S., Perlwitz, J., Shiogama, H., Wehner, M. F., Wolski, P., Cholia, S., Krishnan, H., Murray, D., Angélil, O., Beyerle, U., Ciavarella, A., Dittus, A., Quan, X.-W., and Tadross M.: Experiment design of the International CLIVAR C20C+ Detection and Attribution project, Weather Clim. Extr., 24, 100206, https://doi.org/10.1016/j.wace.2019.100206, 2019.

Sugiyama, M., Shiogama, H., and Emori, S.: Precipitation extreme changes exceeding moisture content increases in MIROC and IPCC climate models, P. Natl. Acad. Sci. USA, 107, 571–575, https://doi.org/10.1073/pnas.0903186107, 2010.

Smith, D. M., Gillett, N. P., Simpson, I. R., Athanasiadis, P. J., Baehr, J., Bethke, I., Bilge, T. A., Bonnet, R., Boucher, O., Findell, K. L., Gastineau, G., Gualdi, S., Hermanson, L., Leung, L. R., Mignot, J., Müller, W. A., Osprey, S., Otterå, O. H., Persad, G. G., Scaife, A. A., Schmidt, G. A., Shiogama, H., Sutton, R. T., Swingedouw, D., Yang, S., Zhou, T., and Ziehn, T.: Attribution of multi-annual to decadal changes in the climate system: The Large Ensemble Single Forcing Model Intercomparison Project (LESFMIP), Front. Clim., 4, 955414, https://doi.org/10.3389/fclim.2022.955414, 2022.

Tatebe, H., Ogura, T., Nitta, T., Komuro, Y., Ogochi, K., Takemura, T., Sudo, K., Sekiguchi, M., Abe, M., Saito, F., Chikira, M., Watanabe, S., Mori, M., Hirota, N., Kawatani, Y., Mochizuki, T., Yoshimura, K., Takata, K., O'ishi, R., Yamazaki, D., Suzuki, T., Kurogi, M., Kataoka, T., Watanabe, M., and Kimoto, M.: Description and basic evaluation of simulated mean state, internal variability, and climate sensitivity in MIROC6, Geosci. Model Dev., 12, 2727–2765, https://doi.org/10.5194/gmd-12-2727-2019, 2019.

Tatebe, H. and Watanabe, M.: MIROC MIROC6 model output prepared for CMIP6 CMIP piControl, Version 20230414, Earth System Grid Federation, [data set], https://doi.org/10.22033/ESGF/CMIP6.5711, 2018a.

Tatebe, H. and Watanabe, M.: MIROC MIROC6 model output prepared for CMIP6 CMIP historical, Version 20230414, Earth System Grid Federation, [data set], https://doi.org/10.22033/ESGF/CMIP6.5603, 2018b.

Thompson, D. W. J., Wallace, J. M., Jones, P. D., and Kennedy, J. J.: Identifying Signatures of Natural Climate Variability in Time Series of Global-Mean Surface Temperature: Methodology and Insights, J. Climate, 22, 6120–6141, 2019.

Timmermann, A., An, S. I., Kug, J. S., Jin, F. F., Cai, W., Capotondi, A., Cobb, K., Lengaigne, M., McPhaden, M., Stuecker, M., Stein, K., Wittenberg, A., Yun, K., Bayr, T., Chen, H., Chikamoto, Y., Dewitte, B., Dommenget, D., Grothe, P., Guilyardi, E., Ham, Y., Hayashi, M., Ineson, S., Kang, D., Kim, S., Kim, W., Lee, J., Li, T., Luo, J., McGregor, S., Planton, Y., Power, S., Rashid, H., Ren, H., Santoso, A., Takahashi, K., Todd, A., Wang, G., Wang, G., Xie, R., Yang, W., Yeh, S., Yoon, J., Zeller, E., and Zhang, X.: El Niño Southern Oscillation complexity, Nature, 559, 535–545, https://doi.org/10.1038/s41586-018-0252-6, 2018.

Trenberth, K. E.: The definition of El Niño, B. Am. Meteorol. Soc., 78, 2771–2778, 1997.

Uhe, P., Mitchell, D., Bates, P. D., Allen, M. R.., Betts, R. A., Huntingford, C., King, A. D., Sanderson, B. M., and Shiogama, H.: Method-uncertainty is essential for reliable confidence statements of precipitation projections, J. Climate, 34, 1227–1240. https://doi.org/10.1175/JCLI-D-20-0289.1, 2021.

Watanabe, M., Dufresne, JL., Kosaka, Y., Mauritsen, T., and Tatebe, H.: Enhanced warming constrained by past trends in equatorial Pacific sea surface temperature gradient, Nat. Clim. Change, 11, 33–37. https://doi.org/10.1038/s41558-020-00933-3, 2021.

Watanabe, M., Shiogama, H., Tatebe, H., Hayashi, M., Ishii, M., and Kimoto, M.: Contribution of natural decadal var.iability to global-warming acceleration and hiatus, Nat. Clim. Change, 4, 893–897, https://doi.org/10.1038/Nclimate2355, 2014.

Wills, R. C. J., Battisti, D. S., Armour, K. C., Schneider, T., and Deser, C.: Pattern Recognition Methods to Separate Forced Responses from Internal Variability in Climate Model Ensembles and Observations, J. Climate, 33, 8693–8719, 2020.

Wu, P., Christidis, N., and Stott, P.: Anthropogenic impact on Earth's hydrological cycle, Nat. Clim Change, 3, 807–810, 2013.

Wyser, K., Koenigk, T., Fladrich, U., Fuentes-Franco, R., Karami, M. P., and Kruschke, T.: The SMHI Large Ensemble (SMHI-LENS) with EC-Earth3.3.1, Geosci. Model Dev., 14, 4781–4796, https://doi.org/10.5194/gmd-14-4781-2021, 2021.